



# Morphometry of Dendritic Materials in Rechargeable Batteries

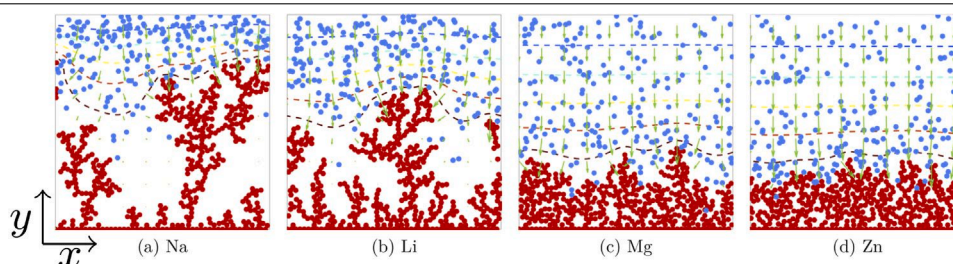
Asghar Aryanfar<sup>a,b,\*</sup>, Sajed Medlej<sup>a</sup>, William A. Goddard III<sup>c</sup>

<sup>a</sup> American University of Beirut, Riad El-Solh, Beirut, 1107, Lebanon

<sup>b</sup> Bahçeşehir University, 4 Çırağan Cad, Beşiktaş, Istanbul, 34353, Turkey

<sup>c</sup> California Institute of Technology, 1200 E California Blvd, Pasadena, CA 91125, United States of America

## GRAPHICAL ABSTRACT



Morphology comparison: red: dendrites, blue: free ions, green vectors: electric fields, dashed lines: isopotential contours.

## ARTICLE INFO

### Keywords:

Dendritic evolution

Electrodeposition

Electrode materials

Reaction probability

## ABSTRACT

The formation of highly-branched dendrites during the charging period of the rechargeable batteries is a critical safety drawback, causing capacity decay in particular during utilization of high energy-density metallic elements as electrode. We develop a comparative framework for predicting the branching tendency of the conventional metallic candidates (*Li, Na, Mg & Zn*) in connection with their inherent material properties as well as representative spatial variants. Our framework covers the kinetic aspect of the electrodeposition, where the brownian motion leads to the formation randomly-branched microstructures. The ionic species are reduced in the proximity of the dendrite body and turn into the atom with the success probability derived from the electron transfer principles. Our development has been carried out in the atomic scale ( $\sim \text{\AA}$ ) and the time interval of inter-ionic collisions ( $\sim \text{ps}$ ) and the determining sub-factors leading to branched evolution are analyzed separately. The results provide intuitive understanding for the effective utilization of the electrode materials in rechargeable batteries based on the given specific application, such as magnitude of the charge carriers, the applied current density or the thickness of the formed microstructures.

## 1. Introduction

The modern era of wireless revolution and portable electronics demands the utilization of reliable intermittent renewables and long-lasting electrical energy storage facilities [1,2]. As well, the growing demand for portable computational power as well as the introduction

of electric vehicles demand novel and reliable high capacity energy storage devices. Despite such impressive growth of the need in the daily lifestyle, the underlying science remains to be developed. Rechargeable batteries, which retrieve/store energy from/within the chemical bonds, have proven to be the most reliable and cleanest resource

\* Corresponding author at: American University of Beirut, Riad El-Solh, Beirut, 1107, Lebanon.

E-mail address: [aryanfar@caltech.edu](mailto:aryanfar@caltech.edu) (A. Aryanfar).

<sup>1</sup> SHE: Standard Hydrogen Electrode, taken conventionally as the reference ( $E_{H^+}^0 = 0$ )

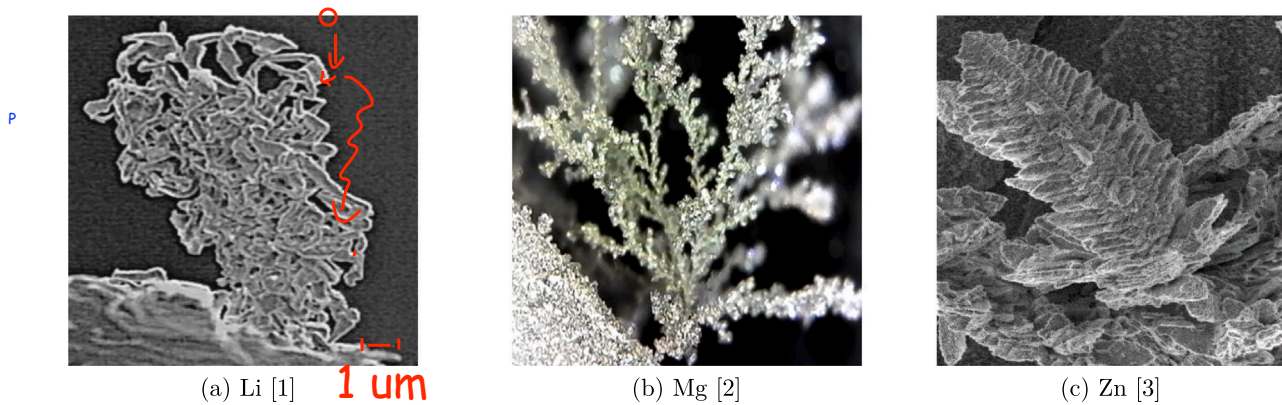


Fig. 1. Dendritic evolution for the demanded electrode materials.

of electrical energy for the efficient management of the power. [3,4] Metallic anodes such as lithium *Li* [5], sodium *Na* [6], magnesium *Mg* [7], and zinc *Zn* [8] are arguably highly attractive candidates for use in high-energy and high-power density rechargeable batteries. Lithium *Li* possess the lowest mass density ( $\rho_{Li} = 0.53 \text{ g cm}^{-3}$ ) and the highest electropositivity ( $E^0 = -3.04 \text{ V vs SHE}^1$ ) which provides the highest gravimetric energy density and likely the highest voltage output, making it suitable for high-power applications such as electric vehicles [9–11]. Sodium has a lower cost and is more earth abundant and is operational for large-scale stationary energy storage applications [12]. Magnesium *Mg* possess a high specific capacity and reactivity [13] whereas Zinc *Zn* is earth-abundant, has low cost and high storage capacity [14].

During the charging, the fast-pace formation of microstructures with relatively low surface energy from Brownian dynamics, leads to the branched evolution with high surface to volume ratio [10]. The quickening tree-like morphologies, examples of which is illustrated in Fig. 1, could occupy a large volume, possibly reach the counter-electrode and short the cell. Additionally, they can also dissolve from their thinner necks during subsequent discharge period and form detached dead crystals, leading to thermal instability and capacity decay [15,16]. Such a formation-dissolution cycle is particularly prominent for the metal electrodes due to lack of intercalation [17], where the depositions in the surface is the only dominant formation mechanism versus the diffusion into the inner layers as the housing [18]. The growing amorphous crystals can pierce into the polymer electrolyte and short the cell afterwards, given their higher porosity, they could have mechanical properties comparable to the bulk form [19].

Previous studies have investigated various factors on dendritic formation such as current density [20], electrode surface roughness [21, 22], impurities [23], solvent and electrolyte chemical composition [24, 25], electrolyte concentration [26], utilization of powder electrodes [27] and adhesive polymers [28], temperature [29,30], guiding scaffolds [31,32], capillary pressure [33], cathode morphology [34] and mechanics [35–38]. Some of conventional characterization techniques used include NMR [39] and MRI. [40] Recent studies also have shown the necessity of stability of solid electrolyte interphase (i.e. SEI) layer for controlling the nucleation and growth of the branched medium [41,42] as well as pulse charging [43–45].

Earlier model of dendrites had focused on the electric field and space charge as the main responsible mechanism [46] while the later models focused on ionic concentration causing the diffusion limited aggregation (DLA). [47–50] Both mechanisms are part of the electrochemical potential [51,52], indicating that each could be dominant depending on the localizations of the electric potential or ionic concentration within the medium. Recent studies have explored both factors and their interplay, particularly in continuum scale and coarser time intervals, matching the scale of the experimental time and space [53].

Table 1

Atomistic properties of the electrode materials.

	<i>Li</i>	<i>Na</i>	<i>Mg</i>	<i>Zn</i>	Ref.	Solvent
$a_M(A^0)^a$	1.45	1.8	1.5	1.35	[60]	Ethylene
$a_{M^{+}}(A^0)$	0.9	1.16	0.86	0.88	[61]	Carbonate
$\phi$ (eV)	2.9	2.4	3.7	4.3	[62]	(EC)

<sup>a</sup> Although the current study is for the amorphous dendritic crystals in mesoscale understanding, the atomic radius has been taken from the natural and ordered crystalline phase:  $a \equiv 2r_{bond}$ .

Other simplified frameworks include phase field modeling [54–56] and analytical developments [57].

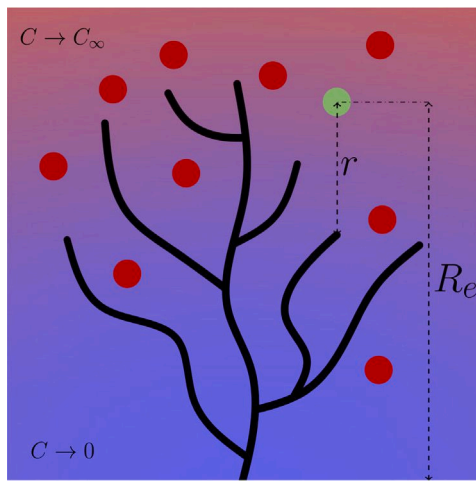
During charge period the ions accumulate at the dendrites tips (unfavorable) due to high electric field in convex geometry and at the same time tend to diffuse away to other less concentrated regions due to diffusion (favorable). Such dynamics typically occurs within the double layer (or stern layer [58]) which is relatively small and comparable to the Debye length. In high charge rates, the ionic concentration is depleted on the reaction sites and could tend to zero [50] nonetheless our continuum-level study extends to larger scale, beyond the double layer region [59].

In this paper, we elaborate further on the tendency of the electrode materials for the formation and growth of dendritic (sub)branches. The candidate elements have already been utilized in primarily<sup>2</sup> batteries with potential applications in rechargeable alternatives. Our atomistic-scale ( $\sim \text{\AA}$ ) approach quantifies the role of the location of ions as spatial variables (Fig. 2(a)) and their connection to the material properties on the kinetics of the ionic transport and electrodeposition (Fig. 2(b)) which leads to the probability of the reaction and hence determines the ultimate form of the metastable dendrites.

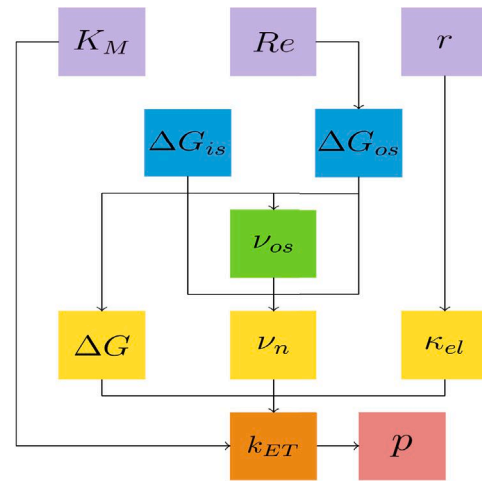
## 2. Methodology

Table 1 shows the atomic scale properties of the electrode materials and Fig. 1 physically represents the ultimate 3 representative morphologies [7,63,64]. The instigation of the dendrites is rooted in the non-uniformity of electrode surface morphology at the atomic scale combined with Brownian ionic dynamics during electrodeposition. Any asperity in the surface provides a sharp electric field that attracts the upcoming ions as a deposition sink. As well the closeness of a convex surface to the counter electrode, as the source of ionic release, would make such peaks more favorable sites, leading to further quickening growth of dendrites in any scale. Such a fast-pace formation leads to the evolution of highly branched medium with a high surface to volume ratio and porosity as high as  $\approx 97\%$  [65].

<sup>2</sup> i.e. non-rechargeable.



(a) Illustration of the spatial variants.  $\{r, R_e, K_m\}$ .



(b) Flowchart of connection to material and solvent properties.

Fig. 2. Schematics of the model parameters and their interconnections. The color of blocks represent the distance they possess in the computational flowchart to the probability of the reaction  $p$ . (For interpretation of the references to color in this figure legend, the reader is referred to the web version of this article.)

The developed model is a combination of the previously-developed Coarse-Grained framework [53] as well as the electron transfer principles based on the Marcus Theory.<sup>3</sup> The approaching ion  $M^{n+}$  to the dendrite body, is successfully deposited to metallic state  $M^0$  with the probability of  $p$  according to the reaction (1):



where  $M \in \{Li, Na, Mg, Zn\}$  and  $n \in \{1, 2\}$ . Respectively, such ion will move on and maintain original form with the probability of  $1 - p$ . Such probability  $p$  directly impacts the rate of electron transfer  $k_{ET}$  as [66]:

$$p = 1 - \exp(-k_{ET}\delta t) \quad (2)$$

where  $\delta t$  is the time interval given for the electron transfer. In fact the reaction probability of  $p$  controls the rate of the electron transfer  $k_{ET}$  in a given try:

$$0 \leq p < 1 \Leftrightarrow 0 \leq k_{ET} < \infty \quad (3)$$

Thus the higher values of  $p$  causes the initial approaches in the outer boundary of the dendrites more successful creating more branches and vice versa smaller probability  $p$  provides more likeliness for the upcoming ions to safely pass the boundary and diffuse into the inner layers, which makes the deposition more compact (i.e. less dendritic).

The rate of electron transfer  $k_{ET}$  in the reaction (2) is expressed from Marcus theory as [51,67]:

$$k_{ET} = K_M \nu_n \kappa_{el} \exp\left(\frac{-\Delta G}{k_B T}\right) \quad (4)$$

where  $K_M$  is the equilibrium constant,  $\nu_n$  is the nuclear frequency factor,  $\kappa_{el}$  is the electron transmission coefficient and  $\Delta G$  is the activation energy (i.e. energy barrier) for the reaction. We address these parameters extensively as below.

### 2.1. Activation energy ( $\Delta G$ )

From Eq. (4) the electron transfer rate  $k_{ET}$  has the highest sensitivity to the energy barrier  $\Delta G$  for the reduction of the ion into the sea of provided electrons within the already-deposited atoms. The energy barrier  $\Delta G$  has two distinct compartments as [66]:

$$\Delta G = \Delta G_{is} + \Delta G_{os} \quad (5)$$

where  $\Delta G_{is}$  and  $\Delta G_{os}$  are the corresponding activation energy for the inner and outer shell electron transfer respectively.

The inner shell activation energy is obtained by assuming the bond as a spring that stretched from ionic to atomic bond length. Such change  $\Delta a$  during transition from ionic  $a_M$  and metallic  $a_{M^{n+}}$  states would be:

$$\Delta a = 2(a_M - a_{M^{n+}}) \quad (6)$$

Therefore the stored inner-shell energy  $\Delta G_{is}$  in general is the sum for all the bonds formed [68] as:

$$\Delta G_{is} = \frac{1}{2} \sum_{i=1}^n f_i \left(\frac{\Delta a}{2}\right)^2 \quad (7)$$

where  $f_i$  is the normal mode force constant and  $n$  is the number of formed bonds during the reduction process. The force constant  $f_i$  can be obtained from the Leonard Jones potential  $V_{LJ}$  relationship given as [69]:

$$V_{LJ} = \epsilon \left[ \left(\frac{a}{r}\right)^{12} - 2 \left(\frac{a}{r}\right)^6 \right]$$

where  $\epsilon$  is the depth of potential well in the energy-distance diagram,  $a$  is the minimum-potential distance (a.k.a bond length), and  $r$  is the distance variable. The force constant  $f$  can be obtained from the second derivative of the potential distribution around the equilibrium distance ( $r \approx a$ ) as<sup>4</sup>:

$$\begin{aligned} f &= \frac{\partial^2 V_{LJ}}{\partial r^2} \Big|_{r=a} = \frac{\partial}{\partial r} \left( \epsilon \left( \frac{-12a^{12}}{r^{13}} + \frac{12a^6}{r^7} \right) \right) \Big|_{r=a} \\ &= 12\epsilon \left( \frac{13a^{12}}{r^{14}} - \frac{7a^6}{r^8} \right) \Big|_{r=a} = \frac{72\epsilon}{a^2} \end{aligned} \quad (8)$$

and the material-dependent parameters are calculated in Table 2. In fact, the bond distance  $a$  is the radial distance  $r$  in the equilibrium condition which occurs in the minimum position of the  $LJ$  potential. The outer shell activation energy  $\Delta G_{os}$  is expressed as [68,70]:

$$\Delta G_{os} = \frac{n^2 e^2}{8} \left( \frac{1}{a} - \frac{1}{R_e} \right) \left( \frac{1}{\epsilon_{opt}} - \frac{1}{\epsilon_s} \right) \quad (9)$$

<sup>4</sup> Equivalent to the energy stored in a spring, stretched infinitesimally to the distance of  $\delta$ , where:  $U = \frac{1}{2} k \delta^2$ , hence the stiffness  $k$  is obtained as  $\frac{\partial^2 U}{\partial \delta^2} = k$ .

<sup>3</sup> The experimental aspect of this work is a part of a future study.

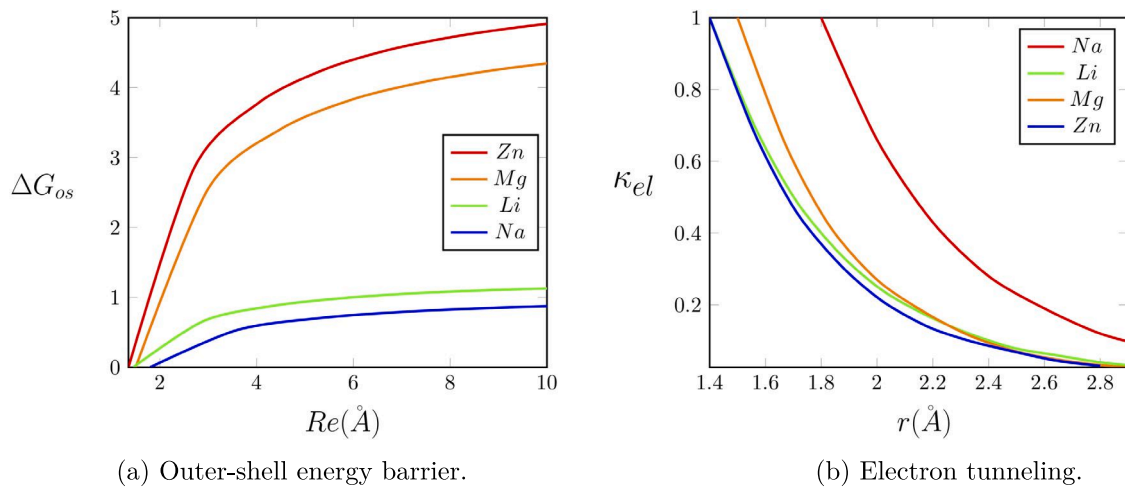


Fig. 3. Distance-dependent variants.

Table 2

General values.

Var.	Li	Na	Mg	Zn	Ref.	Var.	Value	Ref.
$\epsilon$ (meV)	7.1	5.6	0.98	5.4	[71,72]	$\epsilon_s$	95.3	[73]
$\Delta a$ (Å)	1.1	1.28	1.28	0.94	Eq. (6)	$\epsilon_{opt}$	1.84	[74]
$f$ (eV Å)	0.24	0.13	0.03	0.20	Eq. (8)	$\nu_{is}$ (Hz)	$10^{13}$	[68]
$\Delta G_{is}$ (meV)	36.8	26.6	12.3	44.2	Eq. (7)	$\tau_L$ (ps)	0.21	Eq. (14)

where  $e$  is electron charge,  $n$  is valence electrons,  $a$  is the atomic radius,  $R_e$  is the distance of the reaction from the electrode surface and  $\epsilon_{op}$  and  $\epsilon_s$  are optical and static permittivity of the solvent. Fig. 3(a) visualizes the relation of the outer-shell energy barrier  $\Delta G_{os}$  to the distance from the electrode  $R_e$ .

## 2.2. Electron transmission ( $\kappa_{el}$ )

The electronic transmission coefficient represents the probability of electron tunneling as [68]:

$$\kappa_{el} = \kappa_{el}^0 \exp\left(-\frac{4\pi\sqrt{2m_e\phi}}{\hbar}(r-a)\right) \quad (10)$$

where  $\kappa_{el}^0$  is the pre-factor, assumed to be unity for adiabatic processes,  $m_e$  and  $\hbar$  are the electron mass and plank constant,  $r$  is donor-acceptor separation distance,  $a$  is separation distance of closest approach (i.e. interatomic distance), and  $\phi$  is the work function. The tunneling probability is visualized versus distance in Fig. 3(b).

## 2.3. Concentration ratio ( $K_M$ )

The equilibrium constant  $K_M$  represents the ratio of local-to-bulk concentration in the precursor state ( $K_M := \frac{C_{local}}{C_\infty}$ ). Therefore the range of this ratio is:

$$0 \leq K_M \leq 1 \quad (11)$$

During steady-state depletion in the reaction site, such concentration distribution is computed for flat electrodes (i.e. linear distribution) [46,47] as well as curved surfaces [59], reducing from the ambient electrolyte concentration  $C_\infty$  to 0 in redox sites.

## 2.4. Nuclear frequency factor ( $\nu_n$ )

The nuclear frequency factor  $\nu_n$  represents the rates of attempts on the energy barrier  $\Delta G$  and correlates with the bond vibration and

solvent motion. Assuming stagnant solvent in the steady state condition, we can obtain the nuclear frequency factor  $\nu_n$  via quadratic interpolation of activation energies in the inner  $\Delta G_{is}$  and outer  $\Delta G_{os}$  shells as [75]:

$$\nu_n = \sqrt{\frac{\nu_{is}^2 \Delta G_{is} + \nu_{os}^2 \Delta G_{os}}{\Delta G_{is} + \Delta G_{os}}} \quad (12)$$

where  $\nu_{is}$  is the frequency value of attempts in the inner shell, given in Table 2. The frequency of tries on the outer shell  $\nu_{os}$  correlates additionally with the solvent as:

$$\nu_{os} = \tau_L^{-1} \sqrt{\frac{\Delta G_{os}}{4\pi k_B T}} \quad (13)$$

where  $\tau_L$  is the period for the solvent relaxation, scaled from Debye relaxation time  $\tau_D$  as [76]:

$$\tau_L = \frac{\epsilon_\infty}{\epsilon_s} \tau_D \quad (14)$$

where  $\epsilon_\infty$  is the high frequency dielectric constant.

## 2.5. Sample computation

We have utilized the Coarse-grained method in time and space for the simulation of the dendrite morphology [53]. In this context, the electrochemical flux is typically generated either due the gradients of concentration ( $\nabla C$ ) or electric potential ( $\nabla V$ ). The convection is negligible in atomic scale, since Rayleigh number  $Ra$  which is highly dependent on the scale (i.e.  $Ra \propto l^3$ ) is very small for the thin layer of electrodeposition:  $Ra < 1500$  [77]. In the ionic scale, the regions of higher concentration tend to collide and repel more and, given enough time, disperse to lower concentration zones. In the larger scale, such inter-collisions could be added-up and be represented by the diffusion length [59]. Such displacements during the coarse time interval  $\Delta t$  could reach to  $\sim ms$  where the ionic inter-collision time is typically in the order of  $\sim fs$  ( $\Delta t = \sum_{i=1}^n \delta t_i$ ). Therefore, the movement of each ionic specie  $\delta \vec{r}_D$  would be:

$$\delta \vec{r}_D = \sqrt{2D^+ \delta t} \hat{g} \quad (15)$$

where  $D^+$  is the ionic diffusion coefficient in the electrolyte,  $\hat{g}$  is a normalized vector in random direction, representing the Brownian dynamics and the local electric field  $\vec{E}$  is the gradient of electric potential ( $\vec{E} = -\nabla V$ ). The diffusion coefficient  $D^+$  is generally concentration dependent [44], due to electro-neutrality within the considerable space in the domain and we assume it is constant in the range considered. The diffusion length represents the average progress of a diffusive wave in



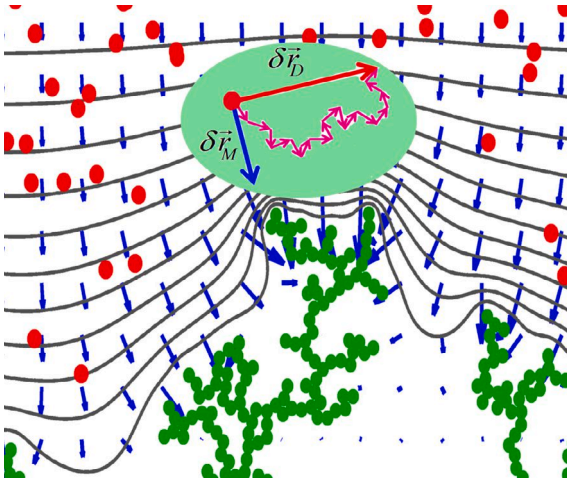


Fig. 4. The transport elements in the coarse scale of time and space. Green: dendrite atoms, red: free ions, blue: electric field, black: iso-potential contours. (For interpretation of the references to color in this figure legend, the reader is referred to the web version of this article.)

a given time  $\Delta t$ , obtained directly from the continuum-scale description of diffusion [78]. On the other hand, ions tend to acquire drift velocity in the electrolyte medium when exposed to electric field and during the given time  $\delta t$  their progress  $\delta \vec{r}_M$  is given as:

$$\delta \vec{r}_M = \mu^+ \vec{E} \delta t \quad (16)$$

where  $\mu^+$  is the mobility of cations in electrolyte,  $\vec{E}$  is the local electric field. Therefore the total effective displacement  $\delta \vec{r}$  is given by:

$$\delta \vec{r} = \delta \vec{r}_D + \delta \vec{r}_M \quad (17)$$

The large-scale movements in Eq. (17) are schematically illustrated in Fig. 4, where the infinitesimal displacements are summed into the coarse grained vector.

Using the material-dependent parameters, given and obtained in Tables 1 and 2 and assuming typical and trivial values for spatial parameters of concentration ratio ( $K_M$ ), the donor-acceptor distance  $r$  and the distance from the electrode  $R_e$  one can reach to the rate of the electron transfer  $k_{ET}$  and the corresponding probability of the reaction  $p$ , which have been provided in Table 3. Combining the evolution dynamics (Eq. (17)) with the description probability of the electron transfer (Eq. (2)) the stochastically grown morphology of the dendritic trees are computed and illustrated in Fig. 5. As well, we define a density measure  $\rho$ , which shows the fraction of filled space in the dendrite zone as:

$$\rho = \frac{N \pi a^2}{4 h_{max} l}$$

where  $N$  is number of atoms in the dendrite body,  $h_{max}$  is the maximum reach of the dendrite atoms from the electrode and  $l$  is the domain scale. The higher values of the density  $\rho$  represent the more favorable and less branched microstructure.

### 3. Results & discussion

The probability of successful jump  $p$ , which in a larger scale controls the rate of electron transfer  $k_{ET}$  is a critical factor in determining the ultimate morphology of the growing dendrites. The higher probability  $p$  causes more successful initial success rates upon reaching the dendrite and the branched morphology is developed from the outer regions (i.e. fingers), whereas the lower probability of jump  $p$  provides more chance for the upcoming ionic species to infiltrate the inner

Table 3

Sample computation parameters.

Var.	Li	Na	Mg	Zn	Ref.	Var.	Value	Ref.
$K_M$	0.5				Eq. (11)	$R_e$ (Å)	5	Fig. 2(a)
$r$ (Å)	2.9	3.6	3.0	2.7	Fig. 2(a)	$\delta t$ (ps)	0.01	[79]
					(~ 2a)			
$\Delta G_{os}$ (meV)	32.6	23.7	124	144	Eq. (9)	$D$ (m <sup>2</sup> /s)	$1.4 \times 10^{-14}$	[53]
$\Delta G$ (meV)	69.4	50.3	137	188	Eq. (5)	$\#Li^+$	50	[53]
$\nu_n$ (THz)	7.4	7.3	4.1	5.6	Eq. (12)	$\#Li^0$	400	[53]
$\kappa_{el}$ ( $\times 10^{-3}$ )	80.0	57.7	52.3	57.1	Eq. (10)	$\Delta t$ (μs)	1	[53]
$k_{ET}$ (GHz)	19.7	29.8	0.527	0.105	Eq. (4)	$l$ (nm)	167	[53]
$p$	0.861	0.949	0.051	0.010	Eq. (2)	$\Delta V$ (mV)	85	[53]

layers of the microstructure and fill the voids, leading to more packed morphology. Therefore:

$$p \uparrow \sim \rho \downarrow \text{ (dendritic)}$$

We have described such probability of success  $p$  in terms of the inherent *material* properties as well as *spatial* variants. While the typical values in Table 3 provides the morphologies illustrated in Fig. 5, we would like to explore the role of each parameters individually for their respective global effect as below.

#### 3.1. Material properties

The underlying attribute of the material, given separately in the Table 1 are described as below. We have explored the most *tangible* material properties which control the other *inter-variables* primarily visualized in Fig. 2(b) as well as the Tables.

##### Work function ( $\phi$ )

The work function  $\phi$  is the minimum thermodynamics work needed to remove an electron from the material to the outer vacuum space [80], and the following order holds between the electrode materials [62]:

$$\phi : Zn > Mg > Li > Na \quad (18)$$

Such property reveals the tendency of the atom to keep the electron before giving away. Thus, the higher value of the work function  $\phi$  leads to lower probability of electron tunneling  $\kappa_{el}$  (Eq. (10), Fig. 3(b)), causing the lower probability of electron transfer  $p$ . Such trend would make less dendritic microstructure, therefore:

$$\phi \uparrow \sim \kappa_{el} \downarrow \sim p \downarrow \text{ (packed)} \quad (19)$$

##### Valence electrons ( $n$ )

The energy barrier needed for the reduction reaction Eq. (1) directly correlates with the valence electrons  $n$  based on the outer-shell activation energy (Eq. (9)), which gives the advantage for the higher valence electron materials as ordered below.

$$n : Zn = Mg > Li = Na \quad (20)$$

Higher valence electrons  $n$  quadratically increase the outer shell activation energy  $\Delta G_{os}$  (Eq. (9)) which is illustrated in Fig. 3(a). Therefore possibility of successful bonding  $p$  is reduced, leading to more packed morphology:

$$n \uparrow \sim \Delta G \uparrow \sim p \downarrow \text{ (packed)} \quad (21)$$

##### Atomic radius ( $a$ )

The size of atom – and the corresponding ion – are effective parameters for the reaction since the large atomic size can instigate higher possibility of overlap and electron transfer. The outer-shell energy barrier  $\Delta G_{os}$  (Eq. (9)) in fact measures the potential energy difference between when the ionic  $M^{n+}$  and metallic  $M$  species reach in the atomic distance  $a$  versus a reference potential, determined by the

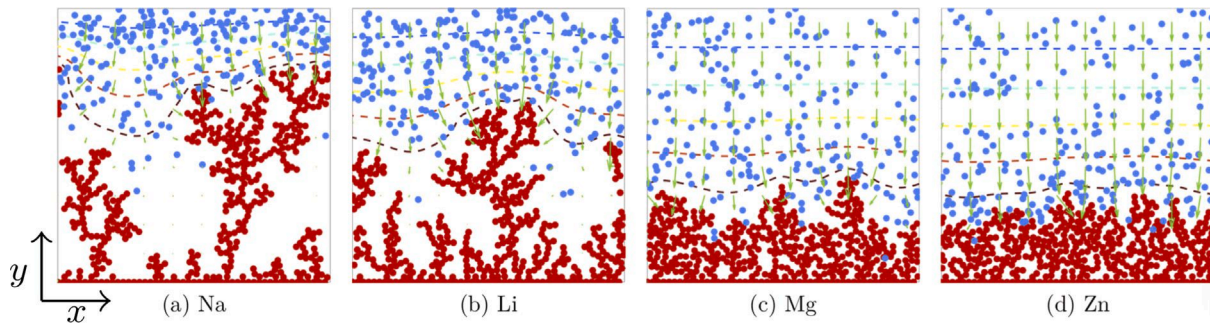


Fig. 5. Obtained morphologies of the electrode materials. Red: dendrites, blue: free ions, green vectors: electric fields, dashed lines: iso-potential contours. (For interpretation of the references to color in this figure legend, the reader is referred to the web version of this article.)

distance from the electrode  $R_e$ . Therefore the bond distance  $a$  directly impact the energy barrier and the materials are ordered as follows:

$$a : Na > Mg > Li > Zn \quad (22)$$

Notably, increasing the overlap possibility due to larger atomic size  $a$  leads to a branched evolution, whereas the smaller atoms could possibly escape more from the branches and infiltrate the inner sites. On the other hand the atomic size  $a$  directly correlates with the probability of the electron tunneling  $\kappa_{el}$  (Eq. (10)). Hence:

$$a \uparrow \sim \kappa_{el} \uparrow, \Delta G \downarrow \sim p \uparrow \text{ (dendritic)} \quad (23)$$

The other size-dependent parameter is the inner-shell activation energy  $\Delta G_{is}$  (Eq. (7)) which is considered as a spring of stiffness  $f$  stretched between the ionic and atomic values  $\Delta a$  (Eq. (6)) and due to symmetry the half value is in effect (i.e.  $\frac{\Delta a}{2}$ ).

Fig. 5 shows that sodium  $Na$  has the highest tendency for the formation of dendritic microstructures. The lower energy barrier of the sodium  $Na$  has previously provided identical insight [81], particularly in the context of surface-diffusion relative to lithium  $Li$  and magnesium  $Mg$  [82,83].

### 3.2. Spatial variants

The spatial variants in Fig. 2(a) and the flowchart 2(b) are location-dependent parameters shown as below.

#### Donor–acceptor distance ( $r$ )

While atoms and ions collide and repel due to Brownian dynamics, the real-time distance  $r$  between the donor and acceptor is a critical parameter which exponentially correlates with the success rate of the electron tunneling  $\kappa_{el}$  (Eq. (10)). The electron from the donor is contained in the atom within the dendrite body shared as part of sea of electrons where the electron acceptor is the ionic specie approaching the dendrite body. Thus:

$$r \uparrow \sim \kappa_{el} \downarrow \sim p \downarrow \text{ (packed)} \quad (24)$$

The exponential behavior of the electron tunneling  $\kappa_{el}$  versus the donor–acceptor distance  $r$  (Fig. 3(b)) finally translates into the probability of successful reaction  $p$  shown in Fig. 6(a). Experiment-wise an important factor controlling the dynamics of the donor–acceptor distance  $r$  can be the current density of the electrodeposition  $j$  (as well as the voltage  $V$ ), where the higher current rate leads to closer distances  $r$  and consequently forms the dendritic trees [21,84,85]. Particularly, during the initiation of dendrites, the ordered lattice crystal structure on the base of deposition could be a source for determining such distance where higher lattice density can provide closer proximity to the upcoming ions. In this manner, the magnesium  $Mg$  provides larger

distances than lithium  $Li$  and leading to a lower migration energy barrier for electron jump [86].

#### Location of the reaction ( $R_e$ )

The distance of the reaction from the electrode surface  $R_e$ , in fact determines the reference potential for the outer shell energy barrier  $\Delta G_{os}$  and therefore the total activation energy  $\Delta G$  (Eq. (5)). In this manner, the further locations from the electrode surface would require higher activation energy  $\Delta G_{os}$  (Eq. (9)) and therefore the probability of electron transfer decreases, leading to more favorable uniform evolution of morphology:

$$R_e \uparrow \sim \Delta G_{os} \uparrow \sim p \downarrow \text{ (packed)} \quad (25)$$

Therefore this factor is favorable for outer regions as illustrated in Fig. 6(b) and the sensitivity location of the reaction  $R_e$  is the highest in regions closer to the electrode (i.e. thin layer deposition).

#### Concentration ratio ( $K_M$ )

As the reaction Eq. (1) occurs, the regions closer to the electrode surface deplete the ions and therefore the concentration is reduced, merely in the double layer region, where it could reach to zero in the limit of current density [46,47,59]. Therefore, starting from the electrode, the ionic concentration will have increasing trend toward ambient electrolyte. Typically the higher concentration leads to the higher rate of interactions and therefore the possibility of electron jump increases, leading to more dendritic morphology [87–90]:

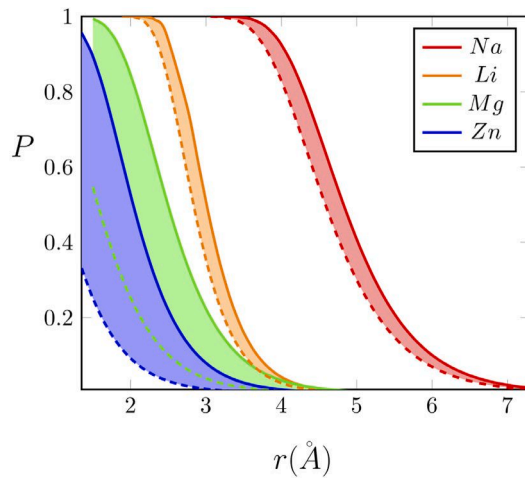
$$K_M \uparrow \sim p \uparrow \text{ (dendritic)} \quad (26)$$

The illustration of the increasing trend is shown in Fig. 7 for the materials considered. Likewise the concentration of the charge carriers correlates directly with the concentration the counter-ions as they both compose the solvent shell [91]. Although the branching factor is similar in all cases ( $\sim 2$ )<sup>5</sup> the branching propensity is higher in the locations further from the surface of the electrode.

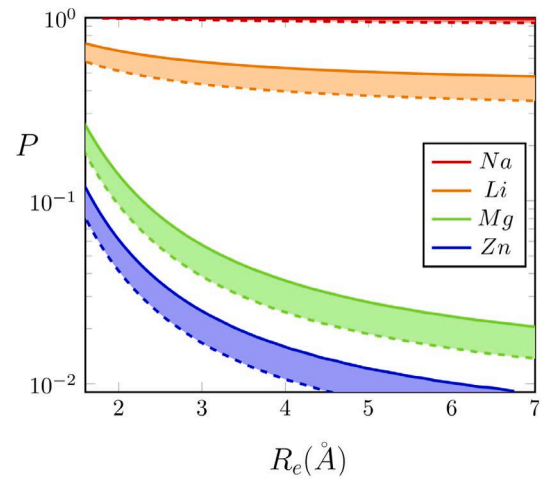
Regarding the fractal behavior, In the range of continuum ( $\sim \mu\text{m}$ ) and higher scales, the ionic concentration and map and the electric field around the branches could possess the same pattern, allowing the formation of fractal morphology and a fractal dimension. However in the smaller and atomic ranges ( $\sim \text{nm}$ ) the evolved morphologies might lose their fractal aspects due to brownian (i.e. stochastic) motion of ions and grow more of amorphous nature. A partial degree of self-organization always exists, since the moving atoms locally get captured in the void zones and tend to group in ordered pattern, assuming the activation energy is provided. Eq. (9) shows that the self-organization can mostly occur in the regions closer to the electrode due to lower outer-shell activation energy  $\Delta G_{os}$ .

The Fig. 8 shows the temporal evolution of the peak of the dendrites. The orders of the materials, which is the same as Fig. 5, follows the

<sup>5</sup> Branching factor is the number of successors generated by a given branch.



(a) Donor-acceptor distance  $r$ :  $R_e = a$ (solid),  $2a$ (dashed),  $K_M = 0.5$ .



(b) Distance from electrode  $R_e$ :  $K_M = 0.5$ (dashed),  $0.75$ (solid),  $r = 2a$ .

Fig. 6. The behavior of reaction probability versus the spatial variables.

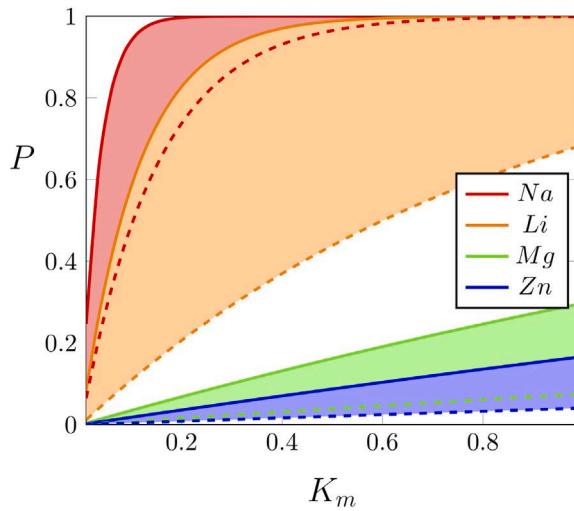


Fig. 7. Probability vs concentration ratio  $K_M$ :  $r = 1.5a$ (dashed),  $2a$ (solid),  $R_e = 2a$ .

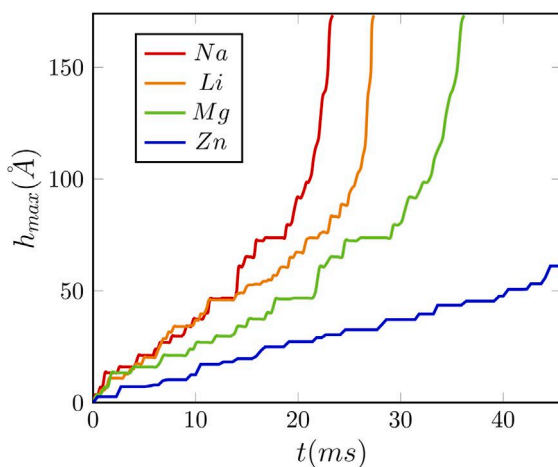


Fig. 8. The temporal evolution of the dendrite height  $h_{max}$ .

Table 4

Experimental equivalent for the analyzed variants.

Variant	$r$	$R_e$	$K_M$
Lab-scale	Applied current	Utilized charge	Concentration $C$
Equivalent	$I$ , Voltage V	$Q$	

probability values obtained in Fig. 3. Additionally, the growth runaway behavior is obvious for three of the fast-growing materials in the time range studied. Additionally, the thermal runaway can qualitatively occur in the most dense sites of the dendrite structure, where the released energy from individual reduction of the atoms can accumulate more effectively and dissipate with a less rate than the rest of the structure.

While this study compares the tendency of the growing dendrites from reaction probability  $p$  perspective. The Solid Electrolyte Interphase  $SEI$ , which prevents the further passivation of the electrolyte as participating agent in the reduction, remains a vital part of the growing interface. Considering the identical electrolyte composition for all cases it should have similar effect on the all materials, leaving the comparisons intact.

Ultimately, the final morphology of the microstructures would depend on the combinatorics effects of the inherent *material* as well as *spatial* properties. The sample computation with the typical values, given in Table 3 shows the order of tendency to grow the dendrites as the following:

$$Na > Li > Mg > Zn$$

However, each discussed individual factor could become dominant in a given circumstance based on the given application. In the experimental scale, the donor-acceptor distance  $r$  correlates with the applied current  $I$  or voltage  $V$  since the higher intensity of charging would get ions closer to each other, the distance from the electrode correlates with the amount of utilized charge  $Q$  since the higher amount of charge can lead to the thicker deposition and therefore the higher distance values from the electrode  $R_e$ , and the concentration variable  $K_M$  correlates directly with the electrolyte concentration  $C_\infty$ . These equivalences to the spatial and physical variants are summarized in Table 4. Gradient comparative study should be valid for the composites with the inclusion of the studied materials, assuming that the other ingredients and the corresponding concentrations are identical. Further works could be on the tuning of  $SEI$  protective layer to manage the interfacial development.



## 4. Conclusions

In this paper, we quantified the amorphous evolution of the dendritic microstructures for the popular electrode materials during the charging of the battery. The density of the electro-deposits which is a measure for the state-of-health, correlates inversely with the probability of successful electron transfer, which is a multi-variable quantity per se. The individual role of the material properties as well as the spatial (i.e. geometric) variants have been analyzed and correlated with the branching tendency. Our framework can be utilized for the selection process of the electrode materials in the given specific application where the prominent factor is either the utilized charge, the applied current density, or the thickness of the electro-deposited films.

### List of Symbols

$a_M, a_{M^{n+}}$	Atomic and ionic radii (Å)
$\phi$	Work function (V)
$p$	Probability of electron transfer ( )
$k_{ET}$	Rate of electron transfer ( $s^{-1}$ )
$K_M$	Local-to-bulk concentration ratio ( )
$\nu_n$	Nuclear frequency factor ( $s^{-1}$ )
$\nu_{is}$	Inner-shell frequency ( $s^{-1}$ )
$\nu_{os}$	Outer-shell frequency ( $s^{-1}$ )
$\kappa_{el}$	Probability of electron tunneling ( )
$\Delta G$	Total activation energy (eV)
$\Delta G_{is}$	Inner-shell energy barrier (eV)
$\Delta G_{os}$	Outer-shell energy barrier (eV)
$k_B$	Boltzmann constant ( $1.38 \times 10^{-23} \text{ m}^2 \text{ kg s}^{-2} \text{ K}^{-1}$ )
$T$	Temperature (298 K)
$D$	Diffusion coefficient ( $\text{m}^2/\text{s}$ )
$C_\infty$	ambient electrolyte concentration (M)
$e$	electron charge (1 eV)
$\tau_L$	Period of solvent relaxation (s)
$\tau_D$	Debye relaxation time (s)
$\epsilon_{op}$	Optical permittivity of solvent ( )
$\epsilon_s$	Static permittivity of solvent ( )
$j$	Current density ( $\text{mA cm}^{-2}$ )
$n$	Valence electrons ( )
$r$	Donor-acceptor distance (Å)
$R_e$	Distance of the reaction from the electrode (Å)
$m_e$	Electron mass ( $9.1 \times 10^{-31} \text{ kg}$ )
$N$	Number of deposited atoms
$\delta t$	Inter-ionic collision time (s)
$\Delta t$	Coarse-scale inter-ionic collision time (s)
$h_{max}$	Maximum reach of the dendrite from the electrode (Å)
$\rho$	The density of the dendrite ( )
$l$	Domain length (Å)
$\hbar$	Planck's constant ( $4.1 \times 10^{-15} \text{ eV s}^{-1}$ )
$\epsilon_0$	Vacuum permittivity ( $e^2 \text{ eV}^{-1} \text{ Å}^{-1}$ )

### CRediT authorship contribution statement

**Asghar Aryanfar:** Conceptualization, Validation, Formal analysis, Investigation, Data curation, Writing - original draft, Writing - review & editing, Visualization, Funding acquisition. **Sajed Medlej:** Methodology, Resources, Software, Writing - review & editing, Supervision, Project administration. **William A. Goddard III:** Consultation, Supervision, Project administration.

### Declaration of competing interest

The authors declare that they have no known competing financial interests or personal relationships that could have appeared to influence the work reported in this paper.

## References

- [1] J. Rugolo, M.J. Aziz, Electricity storage for intermittent renewable sources, *Energy Environ. Sci.* 5 (5) (2012) 7151–7160.
- [2] Bruce Dunn, Haresh Kamath, Jean-Marie Tarascon, Electrical energy storage for the grid: a battery of choices, *Science* 334 (6058) (2011) 928–935.
- [3] Rotem Marom, S. Francis Amalraj, Nicole Leifer, David Jacob, Doron Aurbach, A review of advanced and practical lithium battery materials, *J. Mater. Chem.* 21 (27) (2011) 9938–9954.
- [4] John B. Goodenough, Kyu-Sung Park, The Li-ion rechargeable battery: a perspective, *J. Am. Chem. Soc.* 135 (4) (2013) 1167–1176.
- [5] Xin-Bing Cheng, Rui Zhang, Chen-Zi Zhao, Qiang Zhang, Toward safe lithium metal anode in rechargeable batteries: a review, *Chem. Rev.* 117 (15) (2017) 10403–10473.
- [6] Michael D. Slater, Donghan Kim, Eungje Lee, Christopher S. Johnson, Sodium-ion batteries, *Adv. Funct. Mater.* 23 (8) (2013) 947–958.
- [7] Rachel Davidson, Ankit Verma, David Santos, Feng Hao, Coleman Fincher, Sisi Xiang, Jonathan Van Buskirk, Kelvin Xie, Matt Pharr, Partha P. Mukherjee, et al., Formation of magnesium dendrites during electrodeposition, *ACS Energy Lett.* 4 (2) (2018) 375–376.
- [8] Pucheng Pei, Keliang Wang, Ze Ma, Technologies for extending zinc air batteries cyclelife: A review, *Appl. Energy* 128 (2014) 315–324.
- [9] Siyuan Li, Jixiang Yang, Yingying Lu, Lithium metal anode, in: *Encyclopedia of Inorganic and Bioinorganic Chemistry*, Wiley Online Library, pp. 1–21.
- [10] W. Xu, J.L. Wang, F. Ding, X.L. Chen, E. Nasybutin, Y.H. Zhang, J.G. Zhang, Lithium metal anodes for rechargeable batteries, *Energy Environ. Sci.* 7 (2) (2014) 513–537.
- [11] Aruna Zhamu, Guorong Chen, Chenguang Liu, David Neff, Qing Fang, Zhenning Yu, Wei Xiong, Yanbo Wang, Xiqing Wang, Bor Z. Jang, Reviving rechargeable lithium metal batteries: enabling next-generation high-energy and high-power cells, *Energy Environ. Sci.* 5 (2) (2012) 5701–5707.
- [12] Brian L. Ellis, Linda F. Nazar, Sodium and sodium-ion energy storage batteries, *Curr. Opin. Solid State Mater. Sci.* 16 (4) (2012) 168–177.
- [13] Ivgeni Shterenberg, Michael Salama, Yossi Gofer, Elena Levi, Doron Aurbach, The challenge of developing rechargeable magnesium batteries, *Mrs Bull.* 39 (5) (2014) 453–460.
- [14] Yanguang Li, Hongjie Dai, Recent advances in zinc-air batteries, *Chem. Soc. Rev.* 43 (15) (2014) 5257–5275.
- [15] Kang Xu, Nonaqueous liquid electrolytes for lithium-based rechargeable batteries, *Chem. Rev.-Columbus* 104 (10) (2004) 4303–4418.
- [16] Deepti Tewari, Sobana P. Rangarajan, Perla B. Balbuena, Yevgen Barsukov, Partha P. Mukherjee, Mesoscale anatomy of dead lithium formation, *J. Phys. Chem. C* (2020).
- [17] Zhe Li, Jun Huang, Bor Yann Liaw, Viktor Metzler, Jianbo Zhang, A review of lithium deposition in lithium-ion and lithium metal secondary batteries, *J. Power Sources* 254 (2014) 168–182.
- [18] M.S. Dresselhaus, G. Dresselhaus, Intercalation compounds of graphite, *Adv. Phys.* 30 (2) (1981) 139–326.
- [19] Asghar Aryanfar, Tao Cheng, William A. Goddard, Bulk properties of amorphous lithium dendrites, *ECS Trans.* 80 (10) (2017) 365–370.
- [20] Yaoyu Ren, Yang Shen, Yuanhua Lin, Ce-Wen Nan, Direct observation of lithium dendrites inside garnet-type lithium-ion solid electrolyte, *Electrochem. Commun.* 57 (2015) 27–30.
- [21] Christoffer P. Nielsen, Henrik Bruus, Morphological instability during steady electrodeposition at overlimiting currents, 2015, arXiv preprint arXiv:1505.07571.
- [22] P.P. Natsiavas, K. Weinberg, D. Rosato, M. Ortiz, Effect of prestress on the stability of electrode-electrolyte interfaces during charging in lithium batteries, *J. Mech. Phys. Solids* 95 (2016) 92–111.
- [23] J. Steiger, D. Kramer, R. Monig, Mechanisms of dendritic growth investigated by in situ light microscopy during electrodeposition and dissolution of lithium, *J. Power Sources* 261 (2014) 112–119.
- [24] N. Schweikert, A. Hofmann, M. Schulz, M. Scheuermann, S.T. Boles, T. Hanemann, H. Hahn, S. Indris, Suppressed lithium dendrite growth in lithium batteries using ionic liquid electrolytes: Investigation by electrochemical impedance spectroscopy, scanning electron microscopy, and in situ Li-7 nuclear magnetic resonance spectroscopy, *J. Power Sources* 228 (2013) 237–243.
- [25] Reza Younesi, Gabriel M. Veith, Patrik Johansson, Kristina Edström, Tejs Vegge, Lithium salts for advanced lithium batteries: Li-metal, Li-O 2, and Li-S, *Energy Environ. Sci.* 8 (7) (2015) 1905–1922.
- [26] Soon-Ki Jeong, Hee-Young Seo, Dong-Hak Kim, Hyun-Kak Han, Jin-Gul Kim, Yoon Bae Lee, Yasutoshi Iriyama, Takeshi Abe, Zempachi Ogumi, Suppression of dendritic lithium formation by using concentrated electrolyte solutions, *Electrochem. Commun.* 10 (4) (2008) 635–638.
- [27] I.W. Seong, C.H. Hong, B.K. Kim, W.Y. Yoon, The effects of current density and amount of discharge on dendrite formation in the lithium powder anode electrode, *J. Power Sources* 178 (2) (2008) 769–773.
- [28] G.M. Stone, S.A. Mullin, A.A. Teran, D.T. Hallinan, A.M. Minor, A. Hexemer, N.P. Balsara, Resolution of the modulus versus adhesion dilemma in solid polymer electrolytes for rechargeable lithium metal batteries, *J. Electrochem. Soc.* 159 (3) (2012) A222–A227.



- [29] Asghar Aryanfar, Tao Cheng, Agustin J. Colussi, Boris V. Merinov, William A. Goddard III, Michael R. Hoffmann, Annealing kinetics of electrodeposited lithium dendrites, *J. Chem. Phys.* 143 (13) (2015) 134701.
- [30] Asghar Aryanfar, Daniel J. Brooks, Agustín J. Colussi, Boris V. Merinov, William A. Goddard III, Michael R. Hoffmann, Thermal relaxation of lithium dendrites, *Phys. Chem. Chem. Phys.* 17 (12) (2015) 8000–8005.
- [31] Yuanzhou Yao, Xiaohui Zhao, Amir A. Razzag, Yuting Gu, Xietao Yuan, Rahim Shah, Yuebin Lian, Jinxuan Lei, Qiaoqiao Mu, Yong Ma, et al., Mosaic rGO layer on lithium metal anodes for effective mediation of lithium plating and stripping, *J. Mater. Chem. A* (2019).
- [32] Ji Qian, Yu Li, Menglu Zhang, Rui Luo, Fujie Wang, Yusheng Ye, Yi Xing, Wanlong Li, Wenjie Qu, Lili Wang, et al., Protecting lithium/sodium metal anode with metal-organic framework based compact and robust shield, *Nano Energy* (2019).
- [33] Wei Deng, Wenhua Zhu, Xufeng Zhou, Fei Zhao, Zhaoping Liu, Regulating capillary pressure to achieve ultralow areal mass loading metallic lithium anodes, *Energy Storage Mater.* (2019).
- [34] Alexander W. Abboud, Eric J. Dufek, Boryann Liaw, Implications of local current density variations on lithium plating affected by cathode particle size, *J. Electrochem. Soc.* 166 (4) (2019) A667–A669.
- [35] Markus Klinsmann, Felix E. Hildebrand, Markus Ganser, Robert M. McMeeking, Dendritic cracking in solid electrolytes driven by lithium insertion, *J. Power Sources* 442 (2019) 227226.
- [36] Chen Xu, Zeeshan Ahmad, Asghar Aryanfar, Venkatasubramanian Viswanathan, Julia R. Greer, Enhanced strength and temperature dependence of mechanical properties of Li at small scales and its implications for Li metal anodes, *Proc. Natl. Acad. Sci.* 114 (1) (2017) 57–61.
- [37] Guangyu Liu, Dandan Wang, Jianyu Zhang, Andrew Kim, Wei Lu, Preventing dendrite growth by a soft piezoelectric material, *ACS Mater. Lett.* 1 (5) (2019) 498–505.
- [38] Peng Wang, Wenjie Qu, Wei-Li Song, Haosen Chen, Renjie Chen, Daining Fang, Electro-chemo-mechanical issues at the interfaces in solid-state lithium metal batteries, *Adv. Funct. Mater.* (2019) 1900950.
- [39] Rangeet Bhattacharyya, Baris Key, Hailong Chen, Adam S. Best, Anthony F. Hollenkamp, Clare P. Grey, In situ NMR observation of the formation of metallic lithium microstructures in lithium batteries, *Nature Mater.* 9 (6) (2010) 504.
- [40] S. Chandrashekar, Nicole M. Trease, Hee Jung Chang, Lin-Shu Du, Clare P. Grey, Alexej Jerschow, 7Li MRI of Li batteries reveals location of microstructural lithium, *Nature Mater.* 11 (4) (2012) 311–315.
- [41] Yunsong Li, Yue Qi, Energy landscape of the charge transfer reaction at the complex Li/SEI/electrolyte interface, *Energy Environ. Sci.* (2019).
- [42] Laleh Majari Kasmaee, Asghar Aryanfar, Zarui Chikneyan, Michael R. Hoffmann, Agustín J. Colussi, Lithium batteries: Improving solid-electrolyte interphases via underpotential solvent electropolymerization, *Chem. Phys. Lett.* 661 (2016) 65–69.
- [43] Jun Li, Edward Murphy, Jack Winnick, Paul A. Kohl, The effects of pulse charging on cycling characteristics of commercial lithium-ion batteries, *J. Power Sources* 102 (1) (2001) 302–309.
- [44] S. Chandrashekar, Onyekachi Oparaji, Guang Yang, Daniel Hallinan, Communication 7Li MRI unveils concentration dependent diffusion in polymer electrolyte batteries, *J. Electrochem. Soc.* 163 (14) (2016) A2988–A2990.
- [45] Asghar Aryanfar, Daniel J. Brooks, William A. Goddard, Theoretical pulse charge for the optimal inhibition of growing dendrites, *MRS Adv.* 3 (22) (2018) 1201–1207.
- [46] J.N. Chazalviel, Electrochemical aspects of the generation of ramified metallic electrodeposits, *Phys. Rev. A* 42 (12) (1990) 7355–7367.
- [47] C. Monroe, J. Newman, Dendrite growth in lithium/polymer systems - A propagation model for liquid electrolytes under galvanostatic conditions, *J. Electrochem. Soc.* 150 (10) (2003) A1377–A1384.
- [48] Thomas A. Witten, Leonard M. Sander, Diffusion-limited aggregation, *Phys. Rev. B* 27 (9) (1983) 5686.
- [49] Xin Zhang, Q. Jane Wang, Katharine L. Harrison, Katherine Jungjohann, Brad L. Boyce, Scott A. Roberts, Peter M. Attia, Stephen J. Harris, Rethinking how external pressure can suppress dendrites in lithium metal batteries, *J. Electrochem. Soc.* 166 (15) (2019) A3639–A3652.
- [50] V. Fleury, Branched fractal patterns in non-equilibrium electrochemical deposition from oscillatory nucleation and growth, *Nature* 390 (6656) (1997) 145–148.
- [51] Allen J. Bard, Larry R. Faulkner, *Electrochemical Methods: Fundamentals and Applications*, vol. 2, Wiley, New York, 1980.
- [52] Deepti Tewari, Partha P. Mukherjee, Mechanistic understanding of electrochemical plating and stripping of metal electrodes, *J. Mater. Chem. A* 7 (9) (2019) 4668–4688.
- [53] Asghar Aryanfar, Daniel Brooks, Boris V. Merinov, William A. Goddard III, Agustín J. Colussi, Michael R. Hoffmann, Dynamics of lithium dendrite growth and inhibition: Pulse charging experiments and Monte Carlo calculations, *J. Phys. Chem. Lett.* 5 (10) (2014) 1721–1726.
- [54] Wenyu Mu, Xunliang Liu, Zhi Wen, Lin Liu, Numerical simulation of the factors affecting the growth of lithium dendrites, *J. Energy Storage* 26 (2019) 100921.
- [55] David R. Ely, Aniruddha Jana, R. Edwin García, Phase field kinetics of lithium electrodeposits, *J. Power Sources* 272 (2014) 581–594.
- [56] Daniel A. Cogswell, Quantitative phase-field modeling of dendritic electrodeposition, *Phys. Rev. E* 92 (1) (2015) 011301.
- [57] Rohan Akolkar, Mathematical model of the dendritic growth during lithium electrodeposition, *J. Power Sources* 232 (2013) 23–28.
- [58] Martin Z. Bazant, Brian D. Storey, Alexei A. Kornyshev, Double layer in ionic liquids: Overscreening versus crowding, *Phys. Rev. Lett.* 106 (4) (2011) 046102.
- [59] Asghar Aryanfar, Michael R. Hoffmann, William A. Goddard III, Finite-pulse waves for efficient suppression of evolving mesoscale dendrites in rechargeable batteries, *Phys. Rev. E* 100 (4) (2019) 042801.
- [60] John C. Slater, Atomic radii in crystals, *J. Chem. Phys.* 41 (10) (1964) 3199–3204.
- [61] Robert D. Shannon, Revised effective ionic radii and systematic studies of interatomic distances in halides and chalcogenides, *Acta Crystallogr. Sect. A* 32 (5) (1976) 751–767.
- [62] F.J. Lovas, L.E. Snyder, CRC Handbook of Chemistry and Physics, in: Internet Version 2008, CRC, Boca Raton, FL, 2008, Sect. 14(6).
- [63] F. Orsini, A.D. Pasquier B. Beaudoin J.M. Tarascon, et al., In situ scanning electron microscopy (SEM) observation of interfaces with plastic lithium batteries, *J. Power Sources* 76 (1998) 19–29.
- [64] Kelian Wang, Pucheng Pei, Ze Ma, Huicui Chen, Huachi Xu, Dongfang Chen, Xizhong Wang, Dendrite growth in the recharging process of zinc–air batteries, *J. Mater. Chem. A* 3 (45) (2015) 22648–22655.
- [65] Asghar Aryanfar, Daniel J. Brooks, Tao Cheng, Boris V. Merinov, William A. Goddard, Agustín J. Colussi, Michael R. Hoffmann, Three dimensional modeling of dendrite growth in rechargeable lithium metal batteries, in: Meeting Abstracts, no. 15, The Electrochemical Society, 2015, pp. 1154–1154.
- [66] Rudolph A. Marcus, Norman Sutin, Electron transfers in chemistry and biology, *Biochim. Biophys. Acta* 811 (3) (1985) 265–322.
- [67] Rudolph A. Marcus, On the theory of oxidation-reduction reactions involving electron transfer. I, *J. Chem. Phys.* 24 (5) (1956) 966–978.
- [68] Michael J. Weaver, Redox reactions at metal–solution interfaces, in: Comprehensive Chemical Kinetics, vol. 27, Elsevier, 1988, pp. 1–60.
- [69] John Edward Jones, On the determination of molecular fields II. From the equation of state of a gas, *Proc. R. Soc. Lond. Ser. A Math. Phys. Eng. Sci.* 106 (738) (1924) 463–477.
- [70] James T. Hynes, Outer-sphere electron-transfer reactions and frequency-dependent friction, *J. Phys. Chem.* 90 (16) (1986) 3701–3706.
- [71] Y. Zheng, A. Zaoui, How water and counterions diffuse into the hydrated montmorillonite, *Solid State Ion.* 203 (1) (2011) 80–85.
- [72] Christina Bergonzo, Kathleen B. Hall, Thomas E. Cheatham III, Divalent ion dependent conformational changes in an RNA stem-loop observed by molecular dynamics, *J. Chem. Theory Comput.* 12 (7) (2016) 3382–3389.
- [73] Ralph P. Seward, Ernest C. Vieira, The dielectric constants of ethylene carbonate and of solutions of ethylene carbonate in water, methanol, benzene and propylene carbonate, *J. Phys. Chem.* 62 (1) (1958) 127–128.
- [74] Man Liu, Peter J. Chintali, Xue-bin Huang, Ru-bo Zhang, Structures and dynamic properties of the lip6 electrolytic solution under electric fields—a theoretical study, *Phys. Chem. Chem. Phys.* 21 (24) (2019) 13186–13193.
- [75] R.D. Armstrong, in: J.W. Diggle (Ed.), Oxides and Oxide Films, vol. 2, Marcel Dekker, New York, 1974, (1973).
- [76] Daniel F. Calef, Peter G. Wolynes, Classical solvent dynamics and electron transfer. 1. Continuum theory, *J. Phys. Chem.* 87 (18) (1983) 3387–3400.
- [77] Philip J. Pritchard, John W. Mitchell, John C. Leylegian, Fox and McDonald's Introduction to Fluid Mechanics, Binder Ready Version, John Wiley & Sons, 2016.
- [78] Jean Philibert, One and a half century of diffusion: Fick, Einstein, before and beyond, *Diffusion Fundam.* 4 (6) (2006) 1–19.
- [79] Ron O. Dror, Morten Ø. Jensen, David W. Borhani, David E. Shaw, Exploring atomic resolution physiology on a femtosecond to millisecond timescale using molecular dynamics simulations, *J. Gen. Physiol.* 135 (6) (2010) 555–562.
- [80] Charles Kittel, et al., Introduction to Solid State Physics, vol. 8, Wiley New York, 1976.
- [81] Yuanyue Liu, Boris V. Merinov, William A. Goddard, Origin of low sodium capacity in graphite and generally weak substrate binding of Na and Mg among alkali and alkaline earth metals, *Proc. Natl. Acad. Sci.* 113 (14) (2016) 3735–3739.
- [82] Markus Jackle, Axel Gross, Microscopic properties of lithium, sodium, and magnesium battery anode materials related to possible dendrite growth, *J. Chem. Phys.* 141 (17) (2014) 174710.
- [83] Daniel Stottmeister, Axel Groß, Strain dependence of metal anode surface properties, *ChemSusChem* (2020).
- [84] M. Arakawa, S. Tobishima, Y. Nemoto, M. Ichimura, J. Yamaki, Lithium electrode cycleability and morphology dependence on current-density, *J. Power Sources* 43 (1–3) (1993) 27–35.

- [85] O. Crowther, A.C. West, Effect of electrolyte composition on lithium dendrite growth, *J. Electrochem. Soc.* 155 (11) (2008) A806–A811.
- [86] Ingeborg Treu Røe, Sverre M. Selbach, Sondre Kvalvåg Schnell, Crystal structure influences migration along Li and Mg surfaces, *J. Phys. Chem. Lett.* (2020).
- [87] C. Brissot, M. Rosso, J.N. Chazalviel, S. Lascaud, In situ concentration cartography in the neighborhood of dendrites growing in lithium/polymer-electrolyte/lithium cells, *J. Electrochem. Soc.* 146 (12) (1999) 4393–4400.
- [88] C. Brissot, M. Rosso, J.N. Chazalviel, S. Lascaud, Concentration measurements in lithium/polymer-electrolyte/lithium cells during cycling, *J. Power Sources* 94 (2) (2001) 212–218.
- [89] R.H. Cork, D.C. Pritchard, W.Y. Tam, Local concentration measurements in electrochemical deposition using a schlieren method, *Phys. Rev. A* 44 (1991) 6940–6943.
- [90] R. Feder, Equilibrium defect concentration in crystalline lithium, *Phys. Rev. B* 2 (4) (1970) 828.
- [91] Taylor A. Barnes, Jakub W. Kaminski, Oleg Borodin, Thomas F. Miller III, Ab initio characterization of the electrochemical stability and solvation properties of condensed-phase ethylene carbonate and dimethyl carbonate mixtures, *J. Phys. Chem. C* 119 (8) (2015) 3865–3880.